ACS OMEGA

Open Access

http://pubs.acs.org/journal/acsodf

Article

Carboxymethyl Cellulose/Polyacrylamide/Fe_3O_4 Magnetic Ion Imprinting Biosorbent for Removal and Recovery of La^{3+}

Shuteng Wang,[§] Ming Kong,[§] Wei Li, Enjie Yi, Yan Wang, Minghui Shen, Hao Liu, Shixue Ren, Yuanru Guo, and Jiguo Zhang*

Cite This: *ACS Omega* 2023, 8, 37374−37383

Read Online

ACCESS | Metrics & More | Article Recommendations

ABSTRACT: To use resources rationally, the recovery and recycling of rare earth (RE) from industrial sewage have attracted a lot of attention. Herein, a polymer adsorbent CMC/PAM/Fe_3O_4 (CPF) was synthesized from renewable carboxymethyl cellulose (CMC), polyacrylamide (PAM), and Fe_3O_4 by the template of La^{3+} using ion imprinting technology. The CPF was characterized with X-ray diffraction (XRD), IR, X-ray photoelectron spectroscopy (XPS), and scanning electron microscope (SEM), and results show that PAM and CMC can crosslink with each other and form copolymers with Fe_3O_4 particles dispersing in it. The adsorption properties for the template ions La^{3+} were fully studied. It is found that CPF exhibited good adsorption performance with an adsorption capacity of 34.6 mg·g^{-1}. Cycling experiments show that CPF still has high efficiency even after 5 cycles. Meanwhile, the desorption rate can reach more than 98%. The low wastage and high adsorption/desorption efficiency would enable CPF to be a good candidate adsorbent for removal/recovery of La^{3+} from industrial sewage.

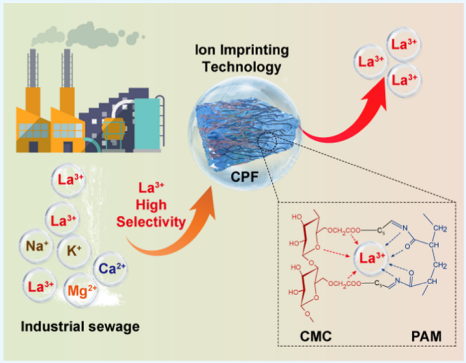

1. INTRODUCTION

Due to their unique and interesting physical and chemical properties, rare earths (REs) have been widely applied in electronic renewable energy, metallurgy, military as well as agriculture.[1,2] The mining, separation, and processing of REs always bring environmental problems. Once RE-contaminated effluent is discharged, it threatens the ecological environment. A large number of studies have reported that REs can accumulate in the bones, liver, and lungs in the human body, which can have detrimental effects on human health.[3] Lanthanum is one of the frequently used REs for making superalloys, catalysts, special glass, and piezoelectric ceramics.[4] Although it has a large range of applications in industrial fields, the challenges associated with the recovery and recycling of lanthanum still remain unresolved.[5] Many methods have been reported for separating lanthanum from industrial effluents,[6] such as solvent extraction,[7] ion exchange,[8] fractional precipitation methods,[9,10] electrokinetic treatment,[11] and adsorption.[12−16] However, high efficiency, low cost, and environmentally friendly methods are still required.

Ion imprinting technology (IIT) is a new separation method developed from molecular imprinting technology (MIT) in recent years.[17] Using this method, target ions are set as the template, and they combine with adsorbents via electrostatic attraction or coordination. After detaching the template ions, the adsorbent would keep the active site, which makes readsorbing target ions feasible. Thus, IIT shows advantages of high selectivity toward the target ions. According to this, many adsorbents are prepared by IIT to deal with a variety of pollutants, especially pollution of metal ions. Among them, polymers are widely adopted as adsorbents due to their ease of forming covalent/coordinate bonds with the target ions. However, most polymers are products of the petrochemical industry, which is nonrenewable and also results in CO_2 emission during processing. There is still a need to search for environmentally friendly polymers that can serve as candidate adsorbents for IIT.

As an abundant, degradable, and renewable polymer, carboxymethyl cellulose (CMC) has gained a lot of attention recently.[18−24] Due to the numerous −COOH and −OH groups in CMC,[18] CMC has more diverse chemical properties compared to cellulose. For example, Yang[25] and co-workers prepared novel millimeter-scale hollow CMC-Al/PEI microspheres by using polyethylenimine (PEI) and glutaraldehyde (GA)-modified CMC-Al, which shows good adsorption performance to methyl blue. In our previous study,[26] we found that CMC is a good biopolymer adsorbent for ITT and

Received: July 19, 2023
Accepted: September 13, 2023
Published: September 25, 2023

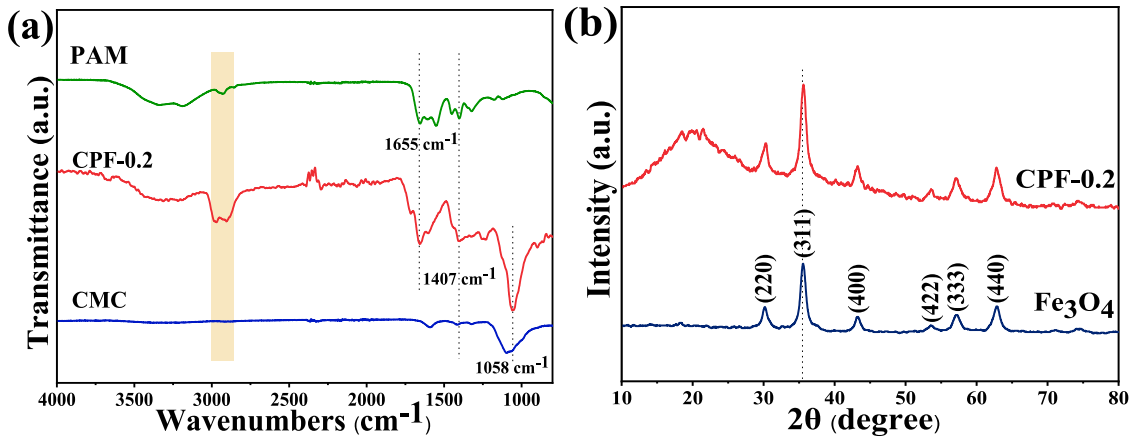

Figure 1. (a) FTIR spectra of PAM, CMC, and CPF-0.2, (b) X-ray diffraction (XRD) patterns of CPF-0.2 and Fe_3O_4.

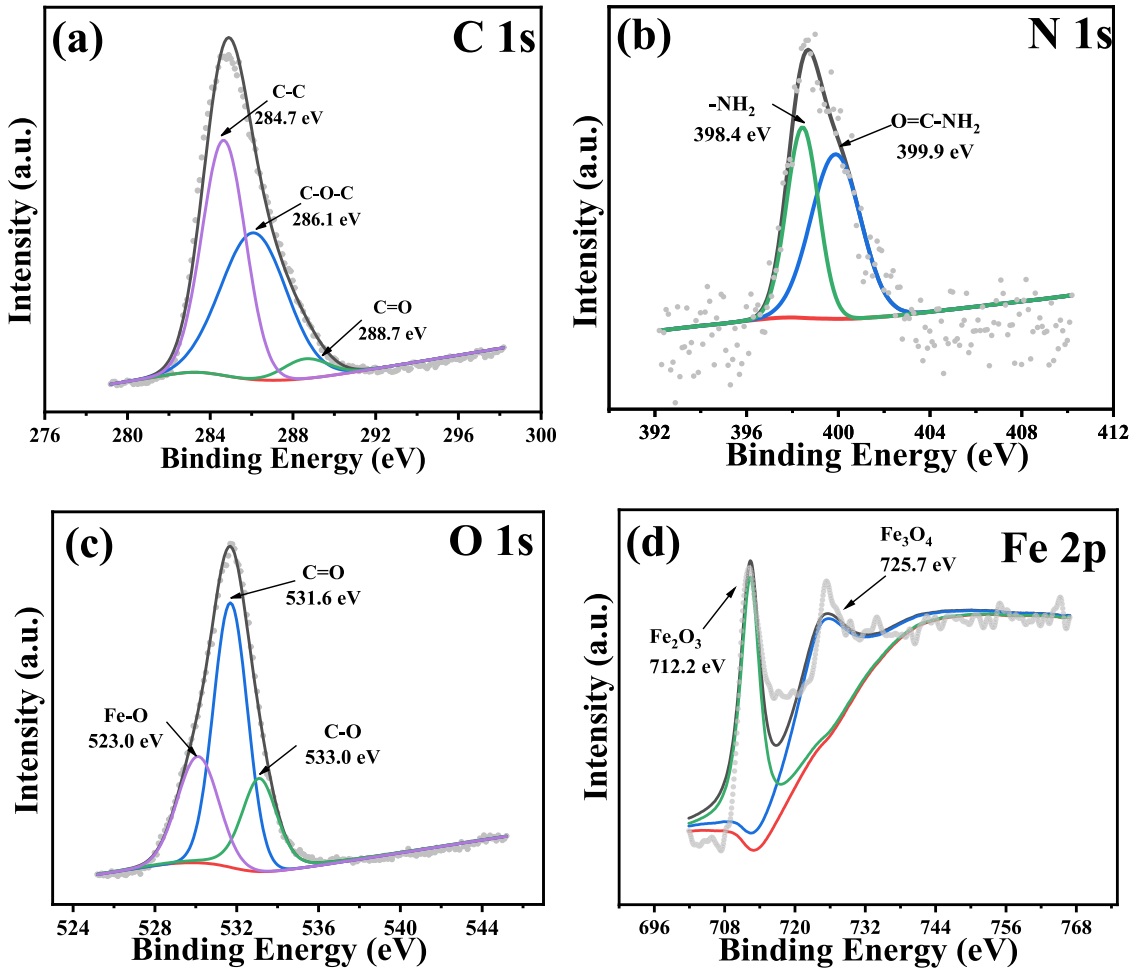

Figure 2. XPS spectra of CPF-0.2: (a) C 1s, (b) N 1s, (c) O 1s, and (d) Fe 2p.

the prepared CMC/Fe_3O_4 shows good adsorption performance to La^{3+}. However, CMC is a water-soluble material, and it would result in a wastage problem during application in water, which would make CMC less efficient during the recycle and reuse process as an adsorbent.

In order to solve this problem, the copolymer CMC/polyacrylamide (PAM) was prepared with magnetic Fe_3O_4 in this work. The prepared CMC/PAM/Fe_3O_4 (CPFs) not only shows high adsorption capacity to La(III) but also shows a high efficiency of recovery and reutilization. Meanwhile, due to its easy separation and environment-friendly properties, the composite material provides the possibility of broadening the applicability of natural polymer materials for the removal/recovery of REs from industrial sewage.

2. RESULTS AND DISCUSSION

2.1. Characterization of CPF. The Fourier transform infrared (FTIR) spectra of CMC, PAM, and CPF are shown in Figure 1a. From the FTIR spectrum of PAM, one can see that peaks at 3319 and 3186 cm^{-1} are associated with N−H

https://doi.org/10.1021/acsomega.3c05192
ACS Omega 2023, 8, 37374−37383

vibrations and peaks at 1662 and 1396 cm^{-1} are associated with C═O and C−N stretching vibrations.[27,28] To CMC, there are three adsorption bands: the first band at 3200−3400 cm^{-1} is the O−H vibration; the second band is the C═O vibration at 1600 cm^{-1}, which has a red-shift due to the strong coupling effect; and the third band located at 1100 cm^{-1} is the C−O−C vibration.[29] Since there are plenty of C−O−C groups in the CMC, this band is relatively stronger. Following the crosslinking of CMC and PAM to form the composite of CPF, the IR spectrum shows functional groups of both CMC and PAM: the peaks at 3658 and 3344 cm^{-1} are attributed to the N−H and O−H stretching vibrations and the peaks at 1716 and 1655 cm^{-1} are attributed to the vibration of C═O. The peak at 1059 cm^{-1} originates from the −C−O unit of the CPF. Compared to the CMC, this vibration has a shift of about 40 cm^{-1} to low frequency, which may be caused by the crosslinking with the large molecule of PAM.

X-ray diffraction (XRD) was used to characterize the structures of samples, as shown in Figure 1b. Diffraction peaks are found at 2θ of 30.32, 35.62, 43.24, 53.44, 57.06, and 62.8° in both CPF-0.2 and Fe_3O_4; they are (220), (311), (400), (422), (333), and (440) planes of the inverse spinel structure of Fe_3O_4 (PDF# 74-0748). Meanwhile, a broad peak at 20−25° belongs to the crosslinked CMC/PAM, indicating the amorphous nature of the CMC/PAM polymers. These results indicated that Fe_3O_4 was successfully combined with CMC/PAM in the composite.

X-ray photoelectron spectroscopy (XPS) was applied to analyze the component of CPF. Figure 2a shows the XPS spectrum of C 1s, which can be fitted into three peaks. Those peaks are the binding energies of C−C (284.7 eV), C−O−C (286.1 eV), and C═O (288.7 eV) of CMC/PAM polymers.[30] The spectrum of N 1s (Figure 2b) can be fitted into peaks at 398.4 and 399.9 eV, which are attributed to $-NH_2$ and O═C-NH_2.[31] In Figure 2c of the O 1s spectrum, the peak at 530.1 eV is the lattice oxygen of Fe−O in Fe_3O_4,[3232] while the peaks at 531.6/533.0 eV are the binding energies of C═O/C−O in the composite.[33] In Figure 2d, Fe 2p is known to consist of $2p_{1/2}$ and $2p_{3/2}$ lines for Fe^{2+} and Fe^{3+} at 725.7 and 712.2 eV,[34−36] indicating the existence of Fe_3O_4 in the composite. The analysis of XPS provides evidence that the composite has the components of Fe_3O_4, CMC, and PAM, and the magnetic copolymer adsorbent has been successfully prepared.

To study the construction of the composite, a scanning electron microscope (SEM) was used to observe the morphology of the samples. As shown in Figure 3a, the prepared Fe_3O_4 particles show uniform sizes of about 200−350 nm, and these particles are significantly agglomerated together. Regarding CPF-0.2, Fe_3O_4 are found well-dispersed in CMC/PAM polymers (Figure 3b). Good dispersivity of the Fe_3O_4 particles endowed the composite with an excellent magnetic property, which would reduce the mass loss of the adsorbent during separation and improve the recycling efficiency.

The effect of different dosages of PAM was also studied, and the SEM results are shown in Figure 3. When 0.05 g of PAM was added, the agglomeration phenomenon of the Fe_3O_4 particles was found in CPF-0.05 (Figure 4a). Meanwhile, the composite shows a morphology characterized by large particles that heap up together. On increasing the content of PAM (Figure 4b−d), the composites display a construction resembling an assembly similar to CPF-0.2, which further indicated that the PAM can crosslink the CMC and form the copolymer. Moreover, the surfaces of these composites

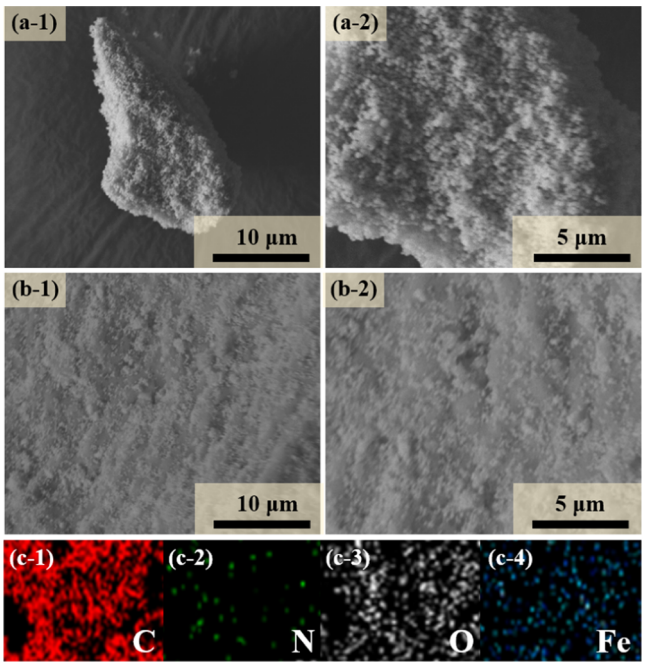

Figure 3. SEM images of Fe_3O_4 (a), CPF-0.2 (b), and energy-dispersive spectrometry (EDS) mapping images of CPF-0.2 (c).

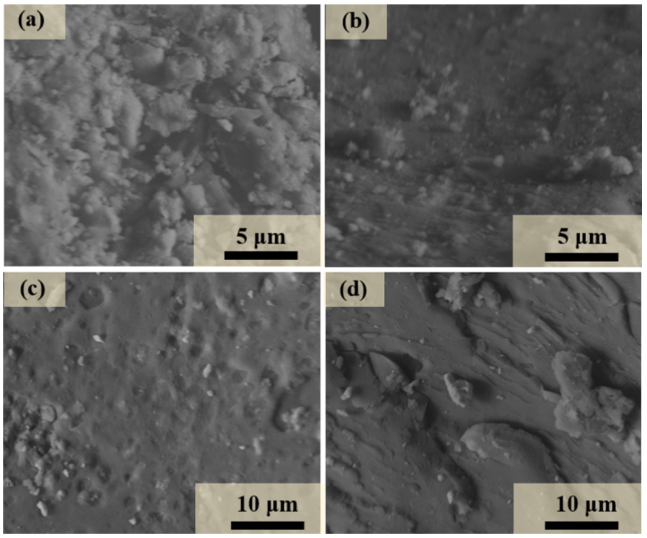

Figure 4. SEM images of CPF-*n*, (a) *n* = 0.05, (b) 0.5, (c) 0.8, and (d) 1.0.

gradually become smooth, which means that the crosslinking degree becomes higher when more PAM is used. This effect also results in Fe_3O_4 particles being buried inside the polymers, making the whole composite look like an assembly. EDS was applied to CPF-0.2, and the mapping images are shown in Figure 3c. It can be seen that the four elements of C, N, O, and Fe are evenly distributed on the surface of the sample. This shows that Fe_3O_4, PAM, and CMC are connected to each other evenly. According to EDS, the contents of C, N, O, and Fe are 57.7, 6.8, 23.6, and 11.9% by weight, respectively, as shown in Table 1. It can be calculated that the content of Fe_3O_4 is about 16.4% in the composite.

2.2. Adsorption Performance. The adsorption performance of prepared CPFs was evaluated by 50 $mg{\cdot}L^{-1}$ La^{3+} and is shown in Figure 5. From Figure 5a, one can see that the

https://doi.org/10.1021/acsomega.3c05192
ACS Omega 2023, 8, 37374−37383

Table 1. Parameters Fitted by Langmuir and Freundlich Models for the Adsorption of La(III)

Langmuir model			Freundlich model		
Q_{max} ($mg·g^{-1}$)	R^2	K_L ($L·mg^{-1}$)	R^2	$1/n$	K_F ($mg·g^{-1}·L^{1/n}·mg^{-1/n}$)
34.6	0.999	0.2	0.970	0.2	13.6

adsorption capacities of CPFs are around 34−35 $mg·g^{-1}$, which means that the adsorption behavior of CPFs was not influenced by the dosage of PAM. This result means that PAM itself has little effect on the adsorption. To consider the cost performance, CPF-0.2 is chosen as the optimal condition as the copolymer adsorbent.

Since the pH of the solution would have a great impact on adsorption performance, the adsorption experiments at different pH values were carried out, and the results are shown in Figure 5b. From Figure 5b, we found that CPF-0.2 has poor performance in low-pH solutions. The reason for this is interference by H^+ in the solution. Although the active sites in CPF were imprinted by La^{3+}, H^+ was still competitive to occupy the active sites in the low-pH condition. This result also suggests that La^{3+} can be eluted and recovered in an acid solution. When increasing the pH value to 4−7, the removal capacity reaches 34.3 $mg·g^{-1}$, indicating the good adsorption performance of CPF in weak-acid and neutral conditions. On continuous increase of the pH to 8, the adsorption capacity reaches 47.1 $mg·g^{-1}$. The increase of adsorption capacity under this condition was caused by the deposition of La^{3+} in alkaline conditions, which enhanced the removal process. Thus, the prepared CPF can be applied in a wide pH range.

2.3. Adsorption Isotherm Studies. The adsorption isotherm of CPF is presented in Figure 6a. It shows that q_e increased quickly with increasing concentrations of La^{3+}. The saturated adsorption capacity (34.3 $mg·g^{-1}$) was reached when the concentration reached 50 $mg·L^{-1}$. Generally, the variation of q_e could be ascribed to the transfer among adsorption sites.[37] There were different types of adsorption sites in ion-imprinted CPFs, such as complete imprinted cavities (CICs), imprinting cavities with some defects (ICDs), and free active loci (FAL) existing in the network. Different adsorption sites result in different adsorption abilities, which compete with each other.[17] The adsorption would first react at the most active sites of CIC and terminate at the weakest sites in FAL. In conditions of a low concentration of La^{3+}, the adsorption was mainly realized by CIC because of the high affinity between CIC and La^{3+}. With the increase in concentration, the adsorption gradually transferred to ICD and FAL, which caused the increased degree of q_e until all active sites were occupied.

Theoretically, when adsorption of La^{3+} happened at low concentrations, all target ions were adsorbed according to the value of q_{max}. However, the q_e at low concentrations did not reach saturation adsorption in the actual experiments. This is because concentration is a significant driving force that can help overcome the mass transfer resistance between the aqueous phase and the solid adsorbent. At low concentrations, the driving force is too weak to make La^{3+} overcome the resistance of mass transfer and reach the adsorbent site.

To fully understand the adsorption process of La(III), the Langmuir (Figure 6b) and Freundlich (Figure 6c) models were applied to fit the isotherm, and the fitted parameters are shown in Table 1. The correlation coefficients (R^2) are 0.999 (Langmuir model) and 0.970 (Freundlich model). This result indicated that the adsorption process is monolayer and chemical adsorption. The q_{max} value calculated by the Langmuir model is 34.6 $mg·g^{-1}$, which is close to the experimental data.

2.4. Adsorption Kinetics of CPF. Figure 7a shows the adsorption kinetic plot of CPF-0.2. It can be seen that the adsorption efficiency of CPF-0.2 is fast within 1 h and reaches equilibrium at about 3 h. The high La(III) adsorption rate of the adsorbent can be attributed to the abundant adsorption sites in CPF, which are uniformly distributed in the composite.

The adsorption processes were evaluated by the pseudo-first-order and pseudo-second-order (Figure 7b,c) models. Between the two models, the pseudo-second-order kinetic model produced the best fit (Table 2), which suggests that the adsorption is mainly dominated by chemical adsorption. This result is consistent with previous descriptions.

To study the applicability of this CPF material for other REs, the adsorption of CPF-0.2 on Ce^{3+}, Pr^{3+}, Nd^{3+}, and Eu^{3+} ions was carried out, and the results are shown in Figure 7d. It can be seen that the adsorption capacities for these four ions are close to each other, and they all fall in the range between 38.4 and 41.1 $mg·g^{-1}$. This is because these rare earth elements

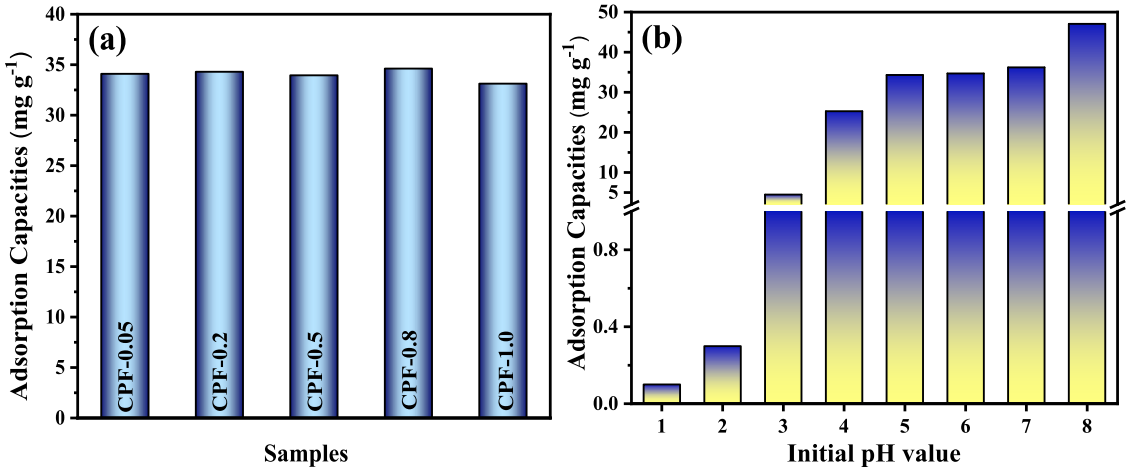

Figure 5. (a) Adsorption capacities of CPFs. (b) pH effect on the adsorption capacities. The adsorption experiment was carried out with 0.1 g of adsorbent dosage in 200 mL of 50 $mg·L^{-1}$ La(III) at a temperature of 25 °C for 420 min.

https://doi.org/10.1021/acsomega.3c05192
ACS Omega 2023, 8, 37374−37383

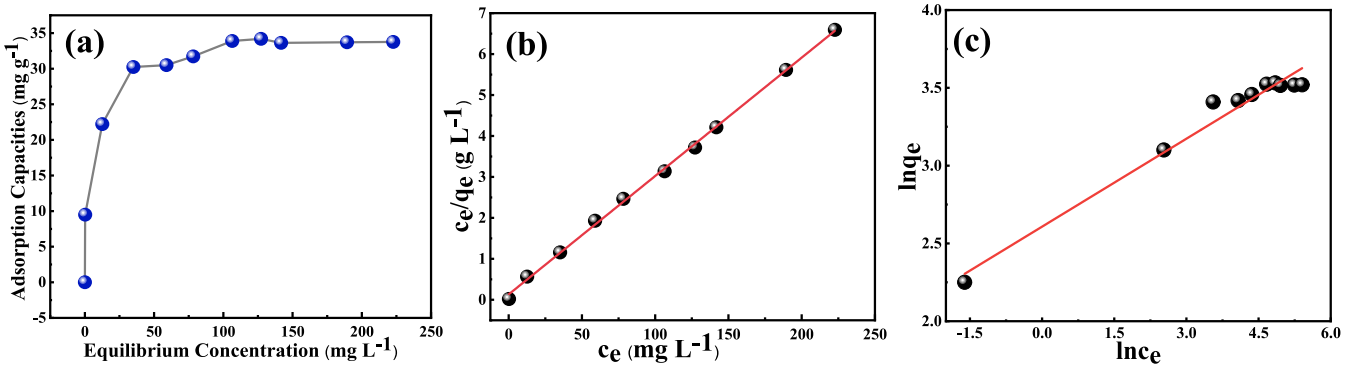

Figure 6. (a) Equilibrium adsorption isotherms of CPF-0.2, (b) adsorption curve fitted by the Langmuir model, and (c) adsorption curve fitted by the Freundlich model.

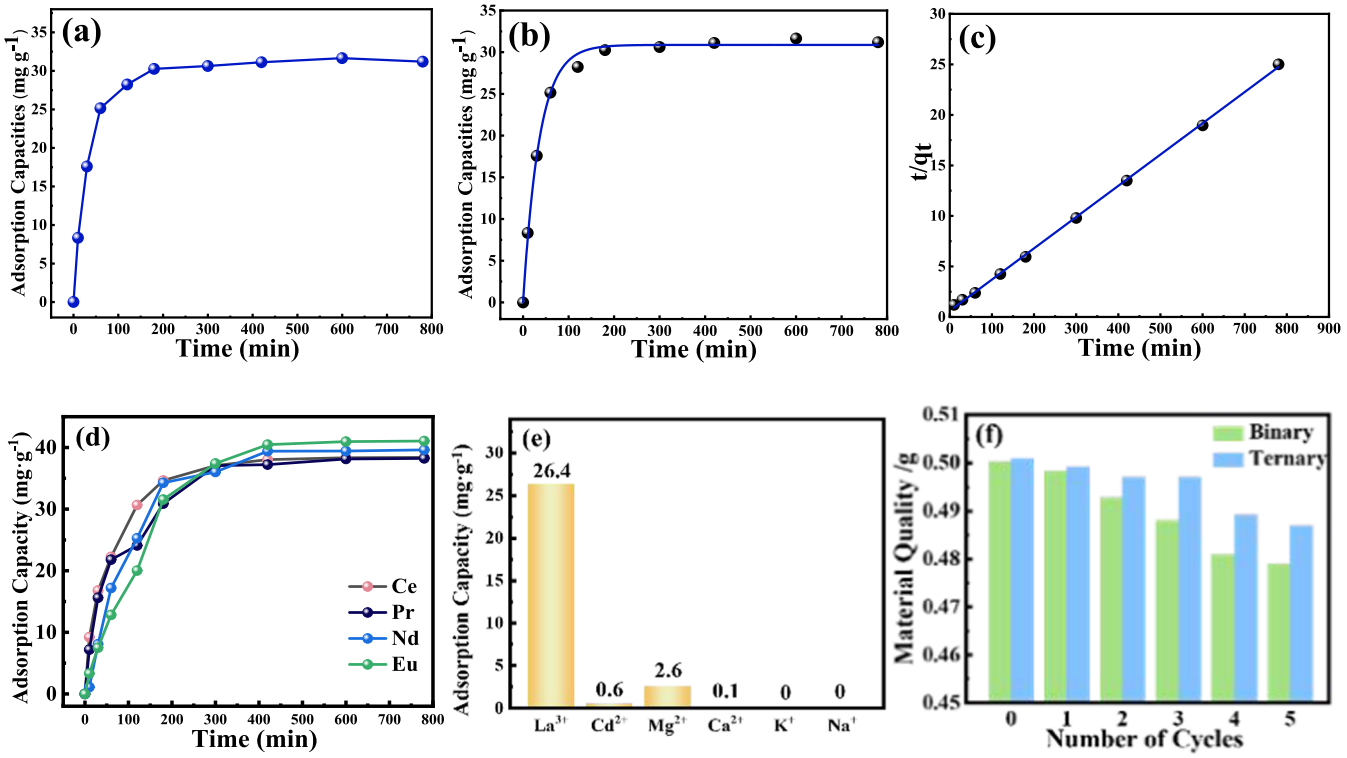

Figure 7. (a) Adsorption kinetic curve of CPF-0.2, (b) fitted plot by the pseudo-first-order kinetic model, and (c) fitted plot by the pseudo-second-order kinetic model. (d) Adsorption kinetics of Ce^{3+}, Pr^{3+}, Nd^{3+}, and Eu^{3+}, (e) adsorption capacities of La^{3+} with interfering ions, and (f) mass quality of CMC/Fe_3O_4 and CMC/PAM/Fe_3O_4 (CPF) during the cycling experiments.

Table 2. Kinetic Constants and Parameters Calculated by the Pseudo-First-Order and Pseudo-Second-Order Kinetic Models

Pseudo-first-order kinetics			Pseudo-second-order kinetics		
$q_{e,calcd}$ ($mg·g^{-1}$)	k_1 (min^{-1})	R^2	$q_{e,calcd}$ ($mg·g^{-1}$)	k_2 ($g·mg^{-1}·min^{-1}$)	R^2
30.9	3.0×10^{-2}	0.996	32.3	2.0×10^{-3}	0.999

have similar charges and properties, which make CPF have a similar adsorption performance to them.

A simulation experiment as the on-spot application was carried out. Ions of Cd^{2+}, Ca^{2+}, Mg^{2+}, K^+, and Na^+ were used as interfering ions. The concentration of each ion is about 50 mg·L^{-1}. The results are listed in Figure 7e. It can be seen that monovalent K^+ and Na^+ have no impact on the adsorption of La^{3+}. However, divalent cations have some impact on the uptake process. Heavy metal ions of Cd^{2+} were adsorbed with the capacity of 0.6 mg·g^{-1}, and the uptake capacity for Mg^{2+} is 2.6 mg·g^{-1}. Despite the presence of competition from divalent cations, the adsorption capacity of La^{3+} still remains at 26.3 mg·g^{-1}, which is about 78% of that obtained in the absence of interfering ions. To test the effect of anions on La^{3+} adsorption, the adsorption experiment with anions of NO_3^-, Cl^-, and SO_4^{2-} was also carried out with a mixture, in which the concentration of each anion was 250 mg·L^{-1}. The capacity of La^{3+} was calculated to be 34.1 mg·g^{-1}, which is very close to that without anions. This result shows that anions have a slight impact on La^{3+} adsorption.

PAM in the composite is used to enhance the crosslink of CMC and then avoid mass loss during application. To prove this, cycling experiments were carried out. After each cycle, the recovered samples were dried and weighed. The masses are listed in Figure 7f. It can be seen from the figure that the mass

https://doi.org/10.1021/acsomega.3c05192
ACS Omega 2023, 8, 37374−37383

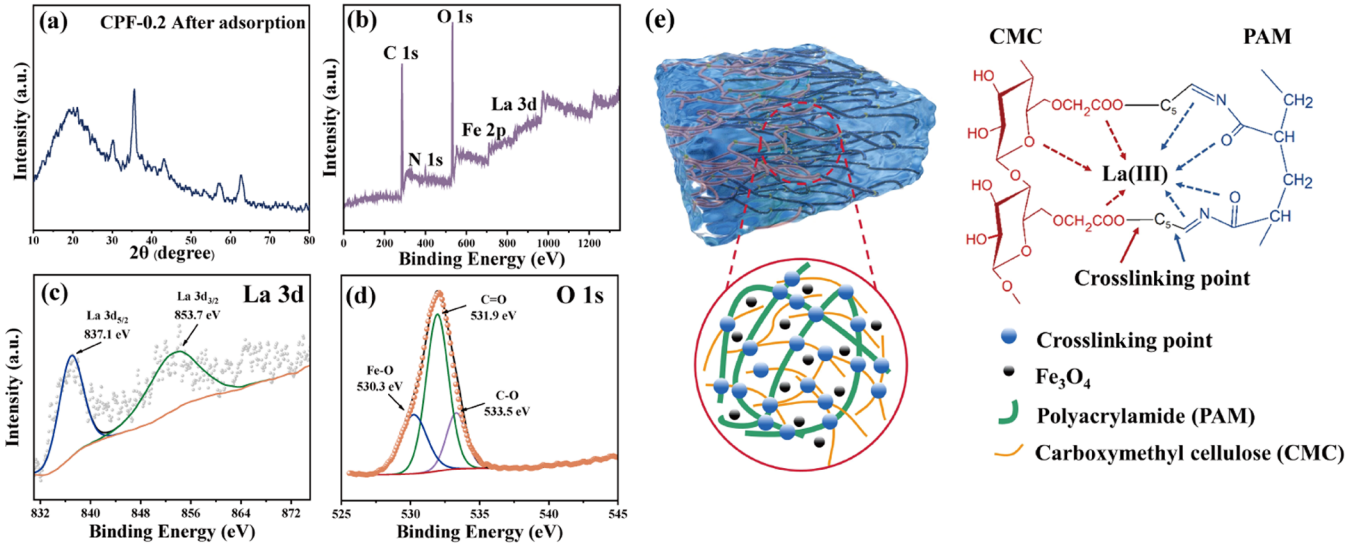

Figure 8. (a) XRD patterns of CPF-0.2 after adsorption; XPS spectra of CPF-0.2 after adsorption: (b) full spectra, (c) La 3d, (d) O 1s, and (e) adsorption mechanism of CPFs.

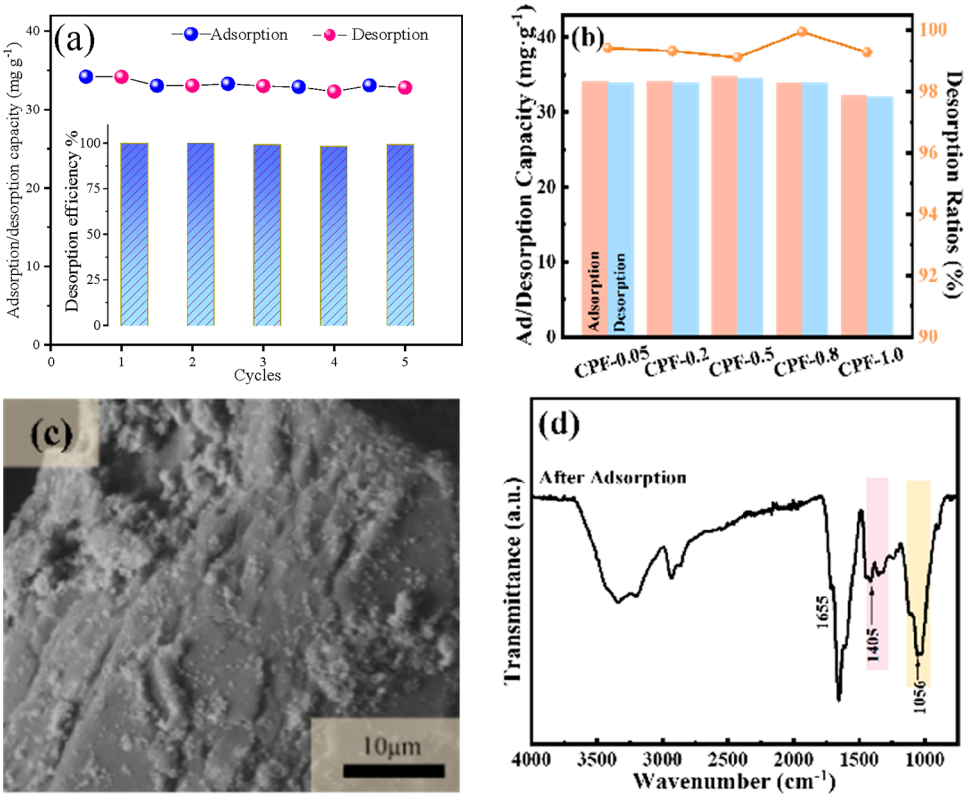

Figure 9. (a) Five cycles of adsorption and desorption of La(III) by CPF-0.2. (b) SEM image of CPF-0.2 after adsorption. (c) Adsorption and desorption efficiencies of CPF with different dosages of PAM. (d) FTIR spectrum of CPF-0.2 after adsorption.

of the ternary system almost did not change in the first 3 cycles and then remained 99% after running for 5 cycles. Regarding CMC/Fe_3O_4, it would retain 95% weight compared to the original one. This result can prove that the addition of PAM in the composite could reduce the loss of adsorbent and make it more efficient and stable.

2.5. Adsorption Mechanism and Reusability of CPF. To further study the adsorption mechanism, XRD and XPS were applied to analyze the CPF after the uptake of La(III) (named CPF-La), and the results are shown in Figure 8. From Figure 8, we can see that the XRD plot of CPF-La has the same pattern as CPF. The sharp diffraction peaks of Fe_3O_4 indicated that the uptake of La^{3+} did not change its CPF structure. The XPS of CPF-La is also presented in Figure 8b–d. From the curves, we can see that La, C, Fe, N, and O are present in CPF-La. In the La 3d spectrum, the peaks located at 837.2 and 853.8 eV can be assigned to La $3d_{5/2}$ and $3d_{3/2}$,[3838] indicating that La^{3+} has been adsorbed on CPF. Meanwhile, the O 1s spectrum shows a little difference compared to that of CPF: the binding energies of both C–O and C═O shifted to a high

https://doi.org/10.1021/acsomega.3c05192
ACS Omega 2023, 8, 37374–37383

energy by 0.3 eV. This phenomenon may be caused by the adsorption of La^{3+}, which changes the chemical environment of oxygen of the $-COO^-$ group during the adsorption process. It can be deduced that La^{3+} adsorbed on the CMC by the functional group of COO^- via electrostatic attraction and formed weak chemical binding. PAM works as a crosslinking agent, which assists in connecting CMC together and gains a high degree of polymerization. A high degree of polymerization would prevent CMC from getting dissolved in water and reduce wastage during application. This also improves the recycling efficiency of CPF. The mechanism scheme is shown in Figure 8e.

According to the advantage of CPF prepared by the IIT method, the reusability for adsorption/desorption was fully studied. It could be observed from Figure 9a that the adsorption capacity of the adsorbent to La^{3+} could reach 33.1 $mg{\cdot}g^{-1}$ even after 5 cycles of adsorption. Moreover, the desorption efficiencies for each cycle are more than 98%.

The effect of PAM dosages on the desorption performance of CPF was also studied. After adsorption, the adsorbents were recovered by a magnet and put into dilute nitric acid for 5 h for desorption. The quantities of adsorbed and desorbed La^{3+} were determined, and the results are shown in Figure 9b. It can be seen that all CPFs have good desorption performance with over 99% desorption efficiency regardless of the dosage of PAM.

The SEM of the recovered CPF also gives almost the same morphology as the fresh CPF, as can be seen in Figure 9c. These results provide evidence that environmental-friendly CPF has good recycling performance when used for removing and recovering La^{3+} from water.[39]

3. CONCLUSIONS

In this work, magnetic ion-imprinted CPFs were prepared by CMC, PAM, and Fe_3O_4, which can be employed to remove and recover La(III) from industrial sewage. The results of FTIR, XRD, and SEM indicate that Fe_3O_4 particles successfully combine with polymers, which enables adsorbents to have a good magnetic property. The prepared CPF shows good adsorption properties to La(III), and the maximum adsorption capacity reaches 34.6 $mg{\cdot}g^{-1}$, as calculated by the Langmuir model. The mechanism study shows that the functional group of COO^- plays an important role in the removal of La(III). Meanwhile, PAM in the composite works as a crosslinking agent, which prevents the CMC from dissolving in water and promotes the efficiency of regeneration. Five recycling experiments also showed that CPF has good reusability and stability. Due to the simple and environmentally friendly adsorption process, CPF would be a promising candidate for La(III) removal/recovery from industrial sewage.

4. EXPERIMENTAL SECTION

4.1. Materials. Carboxymethyl cellulose sodium (CMC, CP) and glutaraldehyde (GA, 50%, CP) were bought from Fuchen Chemical Reagent Co., Ltd. (Tianjin, China). Polyacrylamide (PAM, AR) and lanthanum nitrate hexahydrate ($La(NO_3)_3{\cdot}6H_2O$, 98%, AR) were purchased from FengChuan Chemical Reagent Co., Ltd. (Tianjin, China). Ammonium persulfate (APS, AR) was purchased from J&K Scientific Ltd. (Beijing, China). Nitric acid (HNO_3, AR) was purchased from Beijing Chemical Works. Absolute ethanol (AR) and ethylene glycol (EG, AR) were purchased from Fuyu Fine Chemical Co., Ltd. (Tianjin, China). Ferric chloride ($FeCl_3{\cdot}6H_2O$, AR) and sodium acetate anhydrous (AR) were purchased from Tianli Chemical Reagent Co., Ltd. (Tianjin, China). Trisodium citrate dihydrate (AR) was purchased from Xinbote Chemical Co, Ltd. (Tianjin, China). All of the materials were used without further purification.

4.2. Synthesis of Fe_3O_4 Particles. The Fe_3O_4 particles were synthesized by a solvothermal method used in a previous work with some revisions.[40] 5.0 g of $FeCl_3{\cdot}6H_2O$, 2.0 g of trisodium citrate dihydrate, and 10.0 g of sodium acetate anhydrous were dissolved in 150 mL of EG. The mixture was stirred for 5 h to obtain a brown solution and then transferred into three 100 mL Teflon-lined stainless-steel autoclaves and heated at 200 °C for 10 h. After cooling to room temperature, a black granular product was separated by a magnet and washed with deionized water and absolute ethanol. Finally, Fe_3O_4 was obtained after being dried in a vacuum drying chamber at 45 °C for 24 h.

4.3. Synthesis of CMC/PAM. The free-radical polymerization method was used to synthesize CMC/PAM.[41] 1.0 g of CMC and 0.2 g of PAM were separately dissolved in 50 mL of deionized water with stirring. Then, the CMC solution was heated to 60 °C, and APS was added into it to generate free radicals. After 30 min of heating, the PAM solution was poured into the CMC solution for polymerization reaction for 24 h. Then, the CMC/PAM polymer colloid solution was obtained.

4.4. Preparation of Ion-Imprinted CPFs. 0.1 g of Fe_3O_4 particles (0.1 g) was dispersed in 10 mL of deionized water via ultrasonication. The turbid mixture was then added into 100 mL of a CMC/PAM colloid polymer solution while stirring. After 30 min, 20 mL of 5 $g{\cdot}L^{-1}$ $La(NO_3)_3{\cdot}6H_2O$ and 2 mL of GA were added into the colloid polymer solution. After 1 h stirring, the final mixture was transferred into three Petri dishes and heated at 80 °C for 4 h and 140 °C for 2 h. After drying, the product was fully ground and washed with dilute nitric acid (1:100, volume ratio), absolute ethanol, and deionized water. The ion-imprinted CPF was finally obtained after drying at 70 °C.

To investigate the effect of PAM content, different mass ratios (PAM: CMC = 0.05, 0.5, 0.8, 1.0) were applied to the prepared CPF. In brief, the final samples were labeled as CPF-*n*, *n* = 0.05, 0.2, 0.5, 0.8, and 1.0.

4.5. Batch Adsorption Experiment. *4.5.1. Adsorption Experiment.* The adsorption experiments were carried out as follows: 100 mg of sample was added to 200 mL of solution of 50 $mg{\cdot}L^{-1}$ La^{3+} at 25 °C for 10 h at 120 rpm stirring. Dilute HNO_3 and NaOH were used to regulate the pH of the La^{3+} solutions. During the specified intervals, the solution was sampled, and the concentration of La^{3+} was tested by an inductively coupled plasma mass spectrometer (ICP-MS).

The adsorption capacities were calculated using eq 1. The adsorption kinetics were described using the pseudo-first-order and pseudo-second-order models, corresponding to eqs 2 and 3, respectively. The adsorption isotherm was usually expressed with the Langmuir or Freundlich model, having eqs 4 and 5, respectively.[42−45]

$$q_e = \frac{c_0 - c_t}{m} \times V \quad (1)$$

Here, q_e ($mg{\cdot}g^{-1}$) denotes the adsorption capacity in equilibrium, c_0 and c_t are the initial and final concentrations ($mg{\cdot}L^{-1}$), respectively, and m (g) and V (L) represent the

https://doi.org/10.1021/acsomega.3c05192
ACS Omega 2023, 8, 37374−37383

mass of the adsorbent and the volume of the solution, respectively.

$$q_t = q_e(1 - e^{-k_1 t}) \quad (2)$$

$$\frac{t}{q_t} = \frac{1}{k_2 q_e^2} + \frac{t}{q_e} \quad (3)$$

Here, q_t (mg·g^{-1}) and q_e (mg·g^{-1}) are the adsorption amount versus time t (min) and at equilibrium; k_1 (min^{-1}) and k_2 (g·mg^{-1}·min^{-1}) represent the rate constants of the pseudo-first-order and pseudo-second-order models, respectively.

$$\frac{c_e}{q_e} = \frac{1}{K_L q_{max}} + \frac{c_e}{q_{max}} \quad (4)$$

$$\ln q_e = \ln K_F + \frac{1}{n} \ln c_e \quad (5)$$

Here, c_e (mg·L^{-1}) is the equilibrium concentration and q_e (mg·g^{-1}) is the adsorption amount at equilibrium. q_{max} (mg·g^{-1}) is the maximum adsorption amount, and K_L (L·mg^{-1}) is a Langmuir constant related to the binding energy of the adsorption system. $1/n$ is an empirical parameter in the Freundlich model. K_F (mg·g^{-1}·L$^{1/n}$·mg$^{-1/n}$) and n are related to the Freundlich adsorption constant and the adsorption intensity, respectively.

4.5.2. Ion Interference Experiments. Ions of Cd^{2+}, Ca^{2+}, Mg^{2+}, K^+, and Na^+ have been used as interfering cations, and the concentration of each cation is 50 mg L^{-1} in solution. After 6 h adsorption, the samples were taken and the capacities of each interfering cation were tested. Similarly, Cl^-, NO_3^-, and SO_4^{2-} were used as interfering anions with a concentration of 250 mg L^{-1} for each anion, and the effect of anions on La^{3+} adsorption was also tested with ICP-MAS.

4.5.3. Desorption Experiments. After adsorption, the recovered sample was named CPF-La. The desorption experiments were carried out as follows: CPF-La was dispersed in 200 mL of HNO_3 (1:100, volume ratio) in an incubator-shaker at 25 °C for 10 h. After being separated by a magnet, the solution was sampled, and the concentration of La(III) was tested by ICP-MS. The desorption capacities were calculated using eq 6. Regenerated CPF was washed with deionized water three times and dried before the next cycle of adsorption.

$$q_t = \frac{c_t}{m} \times V \quad (6)$$

Here, q_t (mg·g^{-1}) denotes the desorption capacity in equilibrium, c_t is the final concentration (mg·L^{-1}), and m (g) and V (L) represent the mass of CPF-La and the volume of the HNO_3 solution, respectively.

4.6. Characterizations. The crystal phase of the composites and Fe_3O_4 was analyzed by X-ray diffraction (XRD6100, Shimadzu Corporation) with Cu Kα radiation (wavelength of 1.5418 Å). The morphology was characterized by a scanning electron microscope (SEM). The chemical compositions of samples were measured by X-ray photoelectron spectroscopy (XPS). Infrared spectra were obtained with an FTIR spectrometer (PerkinElmer Instruments Co., Ltd.). The content of La(III) was determined by an inductively coupled plasma mass spectrometer (ICP-MS, PerkinElmer, model Elan9000).

AUTHOR INFORMATION

Corresponding Author

Jiguo Zhang − *Key Laboratory of Bio-Based Material Science & Technology (Ministry of Education), College of Material Science and Engineering, Northeast Forestry University, Harbin 150040, China*; Email: zhangjiguonefu@163.com

Authors

Shuteng Wang − *Key Laboratory of Bio-Based Material Science & Technology (Ministry of Education), College of Material Science and Engineering, Northeast Forestry University, Harbin 150040, China*

Ming Kong − *Key Laboratory of Bio-Based Material Science & Technology (Ministry of Education), College of Material Science and Engineering, Northeast Forestry University, Harbin 150040, China*

Wei Li − *Key Laboratory of Bio-Based Material Science & Technology (Ministry of Education), College of Material Science and Engineering, Northeast Forestry University, Harbin 150040, China*

Enjie Yi − *Key Laboratory of Bio-Based Material Science & Technology (Ministry of Education), College of Material Science and Engineering, Northeast Forestry University, Harbin 150040, China*

Yan Wang − *Harbin Center for Disease Control and Prevention, Harbin 150056, China*

Minghui Shen − *Harbin Center for Disease Control and Prevention, Harbin 150056, China*

Hao Liu − *Key Laboratory of Bio-Based Material Science & Technology (Ministry of Education), College of Material Science and Engineering, Northeast Forestry University, Harbin 150040, China*

Shixue Ren − *Key Laboratory of Bio-Based Material Science & Technology (Ministry of Education), College of Material Science and Engineering, Northeast Forestry University, Harbin 150040, China*; orcid.org/0000-0002-2008-8738

Yuanru Guo − *Key Laboratory of Bio-Based Material Science & Technology (Ministry of Education), College of Material Science and Engineering, Northeast Forestry University, Harbin 150040, China*; orcid.org/0000-0002-9015-4577

Complete contact information is available at: https://pubs.acs.org/10.1021/acsomega.3c05192

Author Contributions

[§]S.W. and M.K. contributed equally to this work.

Author Contributions

We strongly encourage authors to include author contributions and recommend using CRediT for standardized contribution descriptions. Please refer to our general author guidelines for more information about authorship.

Notes

The authors declare no competing financial interest.

ACKNOWLEDGMENTS

This work was funded by the Natural Science Foundations of Heilongjiang Province (C2018006) and the National Undergraduates Training Programs of Innovation (Northeast Forestry University) (grant number 202210225460). The fund of the reformation and development of local universities supported by the central government (2021) is acknowledged.

https://doi.org/10.1021/acsomega.3c05192
ACS Omega 2023, 8, 37374−37383

REFERENCES

(1) Tang, H.; Shuai, W.; Wang, X.; Liu, Y. Extraction of rare earth elements from a contaminated cropland soil using nitric acid, citric acid, and EDTA. *Environ. Technol.* **2017**, *38* (16), 1980−1986.

(2) Huang, Z.; Fan, M.; Tiand, H. Coal and coal byproducts: A large and developable unconventional resource for critical materials-Rare earth elements. *J. Rare Earths* **2018**, *36* (4), 337−338.

(3) Lima, A. T.; Ottosen, L. Recovering rare earth elements from contaminated soils: Critical overview of current remediation technologies. *Chemosphere* **2021**, *265*, No. 129163.

(4) Birungi, Z. S.; Chirwa, E. M. N. The kinetics of uptake and recovery of lanthanum using freshwater algae as biosorbents: Comparative analysis. *Bioresour. Technol.* **2014**, *160*, 43−51.

(5) Li, C.; Ma, H.; Venkateswaran, S.; Hsiao, B. S. Sustainable carboxylated cellulose filters for efficient removal and recovery of lanthanum. *Environ. Res.* **2020**, *188*, No. 109685.

(6) Kegl, T.; Kosak, A.; Lobnik, A.; Novak, Z.; Kralj, A. K.; Ban, I. Adsorption of rare earth metals from wastewater by nanomaterials: A review. *J. Hazard. Mater.* **2020**, *386*, No. 121632.

(7) Tunsu, C.; Menard, Y.; Eriksen, D. O.; Ekberg, C.; Petranikova, M. Recovery of critical materials from mine tailings: A comparative study of the solvent extraction of rare earths using acidic, solvating and mixed extractant systems. *J. Cleaner Prod.* **2019**, *218*, 425−437.

(8) Felipe, E. C. B.; Batista, K. A.; Ladeira, A. C. Q. Recovery of rare earth elements from acid mine drainage by ion exchange. *Environ. Technol.* **2021**, *42* (17), 2721−2732.

(9) Archambo, M. S.; Kawatra, S. K. Extraction of Rare Earths from Red Mud Iron Nugget Slags with Oxalic Acid Precipitation. *Miner. Process. Extr. Metall. Rev.* **2022**, *43* (5), 656−663.

(10) Sinha, S.; Abhilash; Meshram, P.; Pandey, B. D. Metallurgical processes for the recovery and recycling of lanthanum from various resources-A review. *Hydrometallurgy* **2016**, *160*, 47−59.

(11) Maidel, M.; Jeronimo de Santana Ponte, M. J.; Ponte, H. d. A. Recycling lanthanum from effluents of electrokinetic treatment of FCC spent catalyst, using a selective precipitation technique. *Sep. Purif. Technol.* **2019**, *210*, 251−257.

(12) Xu, X.; Zou, J.; Teng, J.; Liu, Q.; Jiang, X.-Y.; Jiao, F.-P.; Yu, J.-G.; Chen, X.-Q. Novel high-gluten flour physically cross-linked graphene oxide composites: Hydrothermal fabrication and adsorption properties for rare earth ions. *Ecotoxicol. Environ. Saf.* **2018**, *166*, 1−10.

(13) Efome, J. E.; Rana, D.; Matsuura, T.; Lan, C. Q. Metal-organic frameworks supported on nanofibers to remove heavy metals. *J. Mater. Chem. A* **2018**, *6* (10), 4550−4555.

(14) Cao, X.; Wang, Q.; Wang, S.; Man, R. A novel polystyrene-poly(hydroxamic acid) interpenetrating polymer network and its adsorption towards rare earth ions*. *J. Rare Earths* **2022**, *40* (1), 127−134.

(15) Zhang, K.-C.; Li, Y.-F.; Liu, Y.; Zhu, Y.; Shi, L.-B. Giant magnetic anisotropy of rare-earth adatoms and dimers adsorbed by graphene oxide. *Phys. Chem. Chem. Phys.* **2017**, *19* (20), 13245−13251.

(16) Rahman, M. L.; Sarjadi, M. S.; Arshad, S. E.; Yusoff, M. M.; Sarkar, S. M.; Musta, B. Kenaf cellulose-based poly(amidoxime) ligand for adsorption of rare earth ions. *Rare Met.* **2019**, *38* (3), 259−269.

(17) Zhang, X.; Jia, W.; Li, D.; Liu, C.; Wang, R.; Li, K.; Li, H.; Chen, Z.; Sun, Y.; Ruso, J. M.; Hu, D.; Liu, Z. Study on synthesis and adsorption properties of ReO_4^- ion imprinted polymer. *J. Polym. Res.* **2020**, *27* (8), 201.

(18) Dong, L.; Jiao, F.; Qin, W.; Zhu, H.; Jia, W. New insights into the carboxymethyl cellulose adsorption on scheelite and calcite: adsorption mechanism, AFM imaging and adsorption model. *Appl. Surf. Sci.* **2019**, *463*, 105−114.

(19) Kong, Q.; Wang, X.; Lou, T. Preparation of millimeter-sized chitosan/carboxymethyl cellulose hollow capsule and its dye adsorption properties. *Carbohydr. Polym.* **2020**, *244*, No. 116481.

(20) Laffleur, F.; Bacher, L.; Vanicek, S.; Menzel, C.; Muhammad, I. Next generation of buccadhesive excipient: Preactivated carboxymethyl cellulose. *Int. J. Pharm.* **2016**, *500* (1−2), 120−127.

(21) Priyadarshi, R.; Kumar, B.; Rhim, J.-W. Green and facile synthesis of carboxymethylcellulose/ZnO nanocomposite hydrogels crosslinked with Zn^{2+} ions. *Int. J. Biol. Macromol.* **2020**, *162*, 229−235.

(22) Tu, C.; Zhang, R.-d.; Yan, C.; Guo, Y.; Cui, L. A pH indicating carboxymethyl cellulose/chitosan sponge for visual monitoring of wound healing. *Cellulose* **2019**, *26* (7), 4541−4552.

(23) Zhao, H.-X.; Wang, Y.; Yang, J.-J.; Zhang, J.-G.; Guo, Y.-R.; Li, S.; Pan, Q.-J. Treatment of heavy metal ions-polluted water into drinkable water: Capture and recovery of Pb^{2+} by cellulose@$CaCO_3$ bio-composite filter via spatial confinement effect. *Chem. Eng. J.* **2023**, *454*, No. 140297.

(24) Bampidis, V.; Azimonti, G.; Bastos, M. d. L.; Christensen, H.; Dusemund, B.; Durjava, M. K.; Kouba, M.; Lopez-Alonso, M.; Puente, S. L.; Marcon, F.; Mayo, B.; Pechova, A.; Petkova, M.; Ramos, F.; Sanz, Y.; Villa, R. E.; Woutersen, R.; Bories, G.; Gropp, J.; Nebbia, C.; Innocenti, M. L.; Aquilina, G.; Subst, E. P. A. P. Safety and efficacy of sodium carboxymethyl cellulose for all animal species. *EFSA J.* **2020**, *18* (7), No. e06211.

(25) Yang, H.-R.; Li, S.-S.; An, Q.-D.; Zhai, S.-R.; Xiao, Z.-Y.; Zhang, L.-P. Facile transformation of carboxymethyl cellulose beads into hollow composites for dye adsorption. *Int. J. Biol. Macromol.* **2021**, *190*, 919−926.

(26) Liu, L.; Chang, S.; Wang, Y.; Zhao, H.; Wang, S.; Zheng, C.; Ding, Y.; Ren, S.; Zhang, J.; Guo, Y.-R. Facile fabrication of ion-imprinted Fe_3O_4/carboxymethyl cellulose magnetic biosorbent: removal and recovery properties for trivalent La ions. *RSC Adv.* **2021**, *11* (41), 25258−25265.

(27) Chen, J.; Wang, D.; Li, X.; Sun, H.; Zhao, H.; Li, Y.; Liu, X.; Shi, G. Photothermal Membrane of CuS/Polyacrylamide−Carboxymethyl Cellulose for Solar Evaporation. *ACS Appl. Polym. Mater.* **2021**, *3* (5), 2402−2410.

(28) Tanwar, A.; Date, P.; Ottoor, D. ZnO NPs incorporated gelatin grafted polyacrylamide hydrogel nanocomposite for controlled release of ciprofloxacin. *Colloid Interface Sci. Commun.* **2021**, *42*, No. 100413.

(29) Peighambardoust, S. J.; Ghergherehchi, E.; Mohammadzadeh Pakdel, P.; Aghdasinia, H. Facile Removal of Methylene Blue Using Carboxymethyl Cellulose Grafted Polyacrylamide/Carbon Black Nanocomposite Hydrogel. *J. Polym. Environ.* **2023**, *31* (3), 939−953.

(30) Sheng, Z.-H.; Shao, L.; Chen, J.-J.; Bao, W.-J.; Wang, F.-B.; Xia, X.-H. Catalyst-Free Synthesis of Nitrogen-Doped Graphene via Thermal Annealing Graphite Oxide with Melamine and Its Excellent Electrocatalysis. *ACS Nano* **2011**, *5* (6), 4350−4358.

(31) Lima, M. C. F. S.; Zaida do Amparo, S.; Ribeiro, H.; Soares, A. L.; Viana, M. M.; Seara, L. M.; Paniago, R. M.; Silva, G. G.; Caliman, V. Aqueous suspensions of carbon black with ethylenediamine and polyacrylamide-modified surfaces: Applications for chemically enhanced oil recovery. *Carbon* **2016**, *109*, 290−299.

(32) Allen, G. C.; Curtis, M. T.; Hooper, A. J.; Tucker, P. M. X-Ray photoelectron spectroscopy of iron−oxygen systems. *J. Chem. Soc., Dalton Trans.* **1974**, No. 14, 1525−1530.

(33) Monyake, K. C.; Alagha, L. Enhanced separation of base metal sulfides in flotation systems using Chitosan-grafted-Polyacrylamides. *Sep. Purif. Technol.* **2022**, *281*, No. 119818.

(34) Grzybek, T.; Klinik, J.; Motak, M.; Papp, H.; Zyla, M. Montmorillonites modified with carbonaceous deposits: I. Formation mechanism and acidity. *J. Colloid Interface Sci.* **2000**, *227* (2), 291−301.

(35) Wang, S.; Zheng, S.; Wang, Z.; Cui, W.; Zhang, H.; Yang, L.; Zhang, Y.; Li, P. Superior lithium adsorption and required magnetic separation behavior of iron-doped lithium ion-sieves. *Chem. Eng. J.* **2018**, *332*, 160−168.

(36) Ge, T.; Jiang, Z.; Shen, L.; Li, J.; Lu, Z.; Zhang, Y.; Wang, F. Synthesis and application of Fe3O4/FeWO4 composite as an efficient and magnetically recoverable visible light-driven photocatalyst for the reduction of Cr(VI). *Sep. Purif. Technol.* **2021**, *263*, No. 118401.

https://doi.org/10.1021/acsomega.3c05192
ACS Omega 2023, 8, 37374−37383

(37) Valderrama, C.; Cortina, J. L.; Farran, A.; Gamisans, X.; Heras, F. X. d. l. Kinetic study of acid red ″dye″ removal by activated carbon and hyper-cross-linked polymeric sorbents Macronet Hypersol MN200 and MN300. *React. Funct. Polym.* **2008**, *68* (3), 718−731.
(38) Yang, L.; Liu, T.; Li, Z.; Liu, C.; Wang, F.; Wu, C. Adsorption of La3+ onto trifluoroacetic acid modified UiO-66-COOH: Adsorption mechanism and application. *Mater. Chem. Phys.* **2023**, *301*, No. 127535.
(39) Tang, L.; Huang, S.; Wang, Y.; Liang, D.; Li, Y.; Li, J.; Wang, Y.; Xie, Y.; Wang, W. Highly Efficient, Stable, and Recyclable Hydrogen Manganese Oxide/Cellulose Film for the Extraction of Lithium from Seawater. *ACS Appl. Mater. Interfaces* **2020**, *12* (8), 9775−9781.
(40) Lv, R.; Jiang, X.; Yang, F.; Wang, Y.; Feng, M.; Liu, J.; Tian, J. Degradable magnetic-response photoacoustic/up-conversion luminescence imaging-guided photodynamic/photothermal antitumor therapy. *Biomater. Sci.* **2019**, *7* (11), 4558−4567.
(41) Peighambardoust, S. J.; Aghamohammadi-Bavil, O.; Foroutan, R.; Arsalani, N. Removal of malachite green using carboxymethyl cellulose-g-polyacrylamide/montmorillonite nanocomposite hydrogel. *Int. J. Biol. Macromol.* **2020**, *159*, 1122−1131.
(42) Godiya, C. B.; Cheng, X.; Li, D.; Chen, Z.; Lu, X. Carboxymethyl cellulose/polyacrylamide composite hydrogel for cascaded treatment/reuse of heavy metal ions in wastewater. *J. Hazard. Mater.* **2019**, *364*, 28−38.
(43) Sun, Y.; Yin, W.-M.; Wang, Y.; Zhao, N.-D.; Wang, X.-Y.; Zhang, J.-G.; Guo, Y.-R.; Li, S.; Pan, Q.-J. Fabrication of ultra-thin MgAl layered double oxide by cellulose templating and its immobilization effect toward heavy metal ions: cation-exchange and deposition mechanism. *Chem. Eng. J.* **2022**, *427*, No. 132017.
(44) Yin, W.-M.; Wang, Y.; Hou, Y.-C.; Sun, Y.; Zhang, J.-G.; Sun, H.-L.; Li, S.-J.; Pan, Q.-J.; Guo, Y.-R. Petaloid-array hierarchically structured carbon Dots/$Mg(OH)_2$ composite: Design, characterization and removal/recovery of cadmium via slowly releasing. *Chem. Eng. J.* **2020**, *401*, No. 125961.
(45) Zhao, N.-D.; Wang, Y.; Zou, X.-H.; Yin, W.-M.; Wang, X.-Y.; Guo, Y.-R.; Pan, Q.-J. Fabrication of cellulose@$Mg(OH)_2$ composite filter via interfacial bonding and its trapping effect for heavy metal ions. *Chem. Eng. J.* **2021**, *426*, No. 130812.

https://doi.org/10.1021/acsomega.3c05192
ACS Omega 2023, 8, 37374−37383